

Article

Effect of Carbon Nanoparticles on the Porous Texture of ι -Carrageenan-Based N-Doped Nanostructured Porous Carbons and Implications for Gas Phase Applications

Samantha K. Samaniego Andrade ¹, Alfréd Menyhárd ¹, Szilvia Klébert ², Miklós Mohai ², Balázs Nagy ³
and Krisztina László ^{1,*}

¹ Department of Physical Chemistry and Materials Science, Faculty of Chemical Technology and Biotechnology, Budapest University of Technology and Economics, 1521 Budapest, Hungary; ssamaniegoandrade@edu.bme.hu (S.K.S.A.); menyhard.alfred@vbk.bme.hu (A.M.)

² Research Centre for Natural Sciences, Institute of Materials and Environmental Chemistry, Eötvös Loránd Research Network, Magyar Tudósok Körútja 2, 1117 Budapest, Hungary; klebert.szilvia@ttk.hu (S.K.); mohai.miklos@ttk.hu (M.M.)

³ H-Ion Research, Development and Innovation Ltd., Konkoly-Thege út 29-33, 1121 Budapest, Hungary; balazs.nagy@hion.hu

* Correspondence: laszlo.krisztina@vbk-bme.hu; Tel.: +36-309-781-999

Abstract: S and N double-doped high surface area biomass-derived carbons were obtained from marine biomass-derived ι -carrageenan. Adding carbon nanoparticles (CNPs), namely graphene oxide (GO) or carbon nanotubes (CNTs), in the early stage of the synthesis leads to a modified porous texture and surface chemistry. The porous textures were characterized by N₂ (−196.15 °C) and CO₂ (0 °C) isotherms. The best GO- and CNT-added carbons had an apparent surface area of 1780 m²/g and 1170 m²/g, respectively, compared to 1070 m²/g for the CNP-free matrix. Analysis of the Raman spectra revealed that CNT was more efficient in introducing new defects than GO. Based on XPS, the carbon samples contain 2–4.5 at% nitrogen and 1.1 at% sulfur. The Dubinin–Radushkevich (DR) and Henry models were used to assess the strength of the interactions between various gases and the surface. The N₂/H₂ and CO₂/CH₄ selectivities were estimated with ideal adsorbed solution theory (IAST). While the CNPs, particularly GO, had a remarkable influence on the porous texture and affected the surface chemistry, their influence on the separation selectivity of these gases was more modest.

Keywords: carbon cryogel; heteroatoms; carbon nanotubes; graphene oxide; gas adsorption



Citation: Andrade, S.K.S.; Menyhárd, A.; Klébert, S.; Mohai, M.; Nagy, B.; László, K. Effect of Carbon Nanoparticles on the Porous Texture of ι -Carrageenan-Based N-Doped Nanostructured Porous Carbons and Implications for Gas Phase Applications. *C* **2023**, *9*, 68. <https://doi.org/10.3390/c9030068>

Academic Editor: Sergey Mikhalovsky

Received: 31 May 2023

Revised: 27 June 2023

Accepted: 3 July 2023

Published: 12 July 2023



Copyright: © 2023 by the authors. Licensee MDPI, Basel, Switzerland. This article is an open access article distributed under the terms and conditions of the Creative Commons Attribution (CC BY) license (<https://creativecommons.org/licenses/by/4.0/>).

1. Introduction

High surface area porous carbon materials have proved to be excellent media for gas phase-related applications, including separation and storage. High surface area and porosity are strongly associated. Carbon materials from renewable biomass provide a sustainable solution for the ever-increasing need for novel porous carbon precursors. While lignocellulosic biomass has long been used as a carbon precursor [1–6], crustacean waste, e.g., crab shells rich in chitosan [7], or plants of marine origin, e.g., seaweed [8], still represent an under-exploited area.

The versatility of porous carbon manufacturing allows the custom making of porous carbons for CO₂ enrichment from gas mixtures with CO₂ content of wide concentration range. Porous carbon materials are competitive adsorbents for the capture of low concentration (~400 ppm) CO₂ from air [9] as well as from flue gas or biogas [10,11] where the CO₂ concentration can be as high as 10–15% and 35–45%, respectively. In the latter case, biomethane (55–65%) is generally the main target of the separation.

Considering porous materials for adsorption-based gas storage or gas separation applications, pores having dimensions similar to the gas molecules of interest are the

most efficient. The diameters of H₂, CO₂, O₂, N₂ and CH₄ are 0.289, 0.33, 0.346, 0.362 and 0.38 nm, respectively [12]. The optimum ratio of pore size to adsorbate molecule size should be in the range of 1.7–3.0 [13], while in membranes, carbon molecular sieves with ultramicropores exhibit enhanced selectivity [14]. Although high micropore volume assures greater gas uptake [15,16], wider pores are not negligible either, as they enhance the dynamics of the transport processes. Physical or chemical activation methods are used to optimize the porous structure [3,17].

In addition to the physical interactions operating in the confinement of the pores, the surface chemistry of the carbon also plays a substantial role in surface interactions and thus in the selectivity. Heteroatoms, e.g., oxygen, nitrogen or sulfur that decorate the entrance and/or the pore walls, tune the hydrophobic/hydrophilic nature of the surface [18], modify the charge distribution of the neighboring carbon atoms [19–21], and thus provide a means to tune the selectivity of the porous carbon. As an example, Lewis basic functionalities (nitrogen and oxygen) present on the carbon surface may attract acidic CO₂ molecules, enhancing their uptake [22,23]. Sevilla et al. reported the synthesis of N-doping activated carbons with high surface area and large CO₂ capture capacity (7.4 mmol/g at 0 °C and 1 bar) [24]. Dual S and N doping results in a large number of carbon atom active sites through the redistribution of spin and charge densities as revealed by density functional theory (DFT) calculations [25].

Carbon nanoparticles (CNPs), like graphene derivatives or carbon nanotubes (CNTs) incorporated into the carbon matrices, may not only tune the porous texture but may create further defects that affect the selective interactions between the gas molecules and the surface. Alhwaige et al. reported that in chitosan–graphene oxide (GO) hybrid aerogels GO affects the apparent surface area and pore size distribution depending on the amount of GO added. An important result was an enhancement of the CO₂ capture capacity of the material with the addition of 20 wt% GO, due to increased surface area and pore volume. In addition, the chitosan–GO hybrid carbon showed enhanced attraction towards CO₂ molecules: -COOH, -OH, -NH₂, -NO₂, -CH₃ groups decorating the surface enhance the CO₂ adsorption by binding to CO₂ due to its quadrupole moment [7]. The computational studies of Bucior et al. found that the high separation selectivity and permeance of carbon nanotubes (CNTs) in the case of H₂/CH₄, CO₂/CH₄ mixtures can be attributed to CH₄ size exclusion [26]. CNP incorporation may also enhance the heat conductivity of the carbon matrix, thus contributing to faster removal of the heat escorting the adsorption process. Earlier, we studied the synthesis of a red algae-based heteroatom-doped carbon. Following the method of Li et al. [27], a highly porous carbon with an apparent surface area close to 1100 m²/g was obtained. Due to the intrinsic S content of the marine biomass-based carrageenan and the N added with urea during the synthesis, a carbon with 5 at% O, 4.6 at% N and at 1% S was obtained. The gas separation and electric energy storage potential of this carbon was recently tested [28]. Here we report the effect of graphene oxide (GO) and multiwalled carbon nanotubes (MWCNT) on the porous texture and surface chemistry of that carrageenan–urea-based carbon matrix. The CNPs were added in the early stage, prior to the gelation of the parent matrix, and are thus expected to tune both the porous texture and the chemistry of the carbons obtained. After characterizing the morphology and surface chemistry, the N₂/H₂ and CO₂/CH₄ selectivity was estimated using ideal adsorbed solution theory (IAST) [29].

2. Materials and Methods

ι-carrageenan powder and urea pearls (98%) were purchased from Sigma Aldrich (Budapest, Hungary). The aqueous GO suspension (0.96 wt%) was prepared from natural graphite (Graphite Týn, Týn nad Vltavou, Czech Republic) following an improved Hummers' method [30,31]. The MWCNT was obtained from Chengdu Organic Chemicals Co., Ltd. (Chengdu, China). The as-received CNTs were oxidized in cc. HNO₃ (65%) for 3 h at 80 °C, washed with aqueous NaOH and reprotonated with 1.0 M HCl before use [32]. All other chemicals were used without further purification. Hydrogel matrices were ob-

tained by mixing 2 g urea and 2 g ι -carrageenan with a 100 mL aqueous CNP suspension (containing 50, 100 and 200 mg of the corresponding nanoparticles, respectively) at 80 °C. The freeze-dried polymer cryogels were pyrolyzed in a rotary quartz reactor at 700 °C (20 °C/min) in dry N₂ flow (25 L/h) for 1 h. The remaining inorganic impurities were removed by washing with 1.0 M HCl prior to annealing in Ar flow for 1 h at 1000 °C. The dry polymer and carbon cryogels were labelled PA and CA, respectively. The sample labels also refer to the incorporated CNP (as GO or CNT) and their incorporated mass (50, 100 or 200), respectively. CNP-free polymer and carbon gels were prepared for comparison [28].

2.1. Characterization Methods

Thermogravimetric analysis was performed on 2–10 mg polymer samples using a TGA 6 (Perkin Elmer, Waltham, MA, USA) thermogravimetric analyzer following a heating rate of 1.5 °C/min from room temperature up to 300 °C, and then 10 °C/min from 300 °C to 900 °C in nitrogen (20 mL/min).

Scanning electron micrographs were taken by a Zeiss Sigma 300 field emission scanning electron microscope (FESEM) (Carl Zeiss QEC GmbH, Oberkochen, Germany). Low temperature (−196.15 °C) nitrogen adsorption measurements were performed after 24 h degassing at 110 °C in a NOVA 2000 e (Quantachrome, Boynton Beach, FL, USA) instrument. The apparent surface area S_{BET} was determined using the Brunauer–Emmett–Teller (BET) model [33]. The pore volume $V_{0.98}$ was estimated from the amount of vapor adsorbed at $p/p_0 = 0.98$, assuming that the adsorbed gas fills the corresponding pores as liquid. The Dubinin–Radushkevich (DR) model [34] was used to calculate the micropore volume W_0 . The slope of the DR plots as well as the Henry constant (the initial slope of the isotherms) were used to characterize the interaction between the carbon surface and the adsorbate. The pore size distributions were computed using quenched solid density functional theory (QSDFT) for slit/cylindrical pore geometry [35]. Carbon dioxide adsorption was measured at 0 °C up to atmospheric pressure with an AUTOSORB-1 (Quantachrome, USA) analyzer. The pore size distribution in the ultramicropore range was derived by nonlinear density functional theory (NLDFT). Evaluation of the primary adsorption data was performed with the Quantachrome ASiQwin software (version 3.0). Raman spectra were obtained using a LabRAM (Horiba Jobin Yvon, Palaiseau, France) instrument. The laser source was a $\lambda = 532$ nm Nd-YAG (15 mW laser power at the focal point). A 0.6 OD filter was used to reduce the power of the beam. Parameter optimization and data analysis were performed by LabSpec 5 software.

X-ray photoelectron spectra were recorded on a Kratos XSAM 800 spectrometer operating in fixed analyzer transmission mode, using Mg K _{α 1,2} (1253.6 eV) excitation. The analysis chamber pressure was below 1×10^{-7} Pa. Survey spectra were recorded in the range 150–1300 eV in 0.5 eV steps. The photoelectron lines of C1s, O1s, N1s and S2p were measured in 0.1 eV steps with 1 s dwell time. The spectra were referenced to the energy of the C1s line of sp² type graphitic carbon, set at 284.3 ± 0.1 eV binding energy (BE). Peak decomposition was performed after Shirley-type background removal using a Gaussian–Lorentzian peak shape with 70:30 ratio as reported elsewhere [36]. Quantitative analysis, based on integrated peak intensity, was performed by the XPS MultiQuant program [37], applying the conventional infinitely thick layer model using the experimentally determined photoionization cross-section data of Evans et al. [38] and the asymmetry parameters of Reilman et al. [39]. Attenuated total reflectance Fourier transform infrared (FTIR-ATR) spectra were recorded on powdered carbons in the range 4000–400 cm^{−1} at a resolution of 4 cm^{−1} by 64 scans using a Tensor 27 (Bruker Optik GmbH, Leipzig, Germany) spectrophotometer equipped with a Platinum ATR unit A225. For the background signal, the measured medium was air. Since the absorption of the powders was very strong, a moderate polynomial baseline correction and smoothing were applied.

2.2. Adsorption with Probe Gases

Nitrogen ($-196.15\text{ }^{\circ}\text{C}$), carbon dioxide and methane (both at $0\text{ }^{\circ}\text{C}$) isotherms were measured up to atmospheric pressure in a NOVA 2000 e (Quantachrome, USA) volumetric instrument. An Autosorb 1C (Quantachrome, Boynton Beach, FL, USA) volumetric instrument was used to perform hydrogen sorption experiments with high purity hydrogen (99.999%) at $-196.15\text{ }^{\circ}\text{C}$. IAST [29] was used to assess the gas separation selectivity of the carbons studied.

3. Results and Discussion

3.1. Effect of the CNPs on the Morphology and Chemistry of the Samples

Figure 1 presents the thermogravimetric curve of the CNP-free and the 50 mg GO- and CNT-loaded polymer samples. The TG curves have multistep behavior with weight losses at similar temperatures, indicating that the thermal decomposition is governed by the pristine polymer. GO and CNT have little influence at these concentrations. The slightly different effect of the CNPs may stem from their dissimilar oxygen content (30 at% and 5 at% for GO and CNT, respectively).

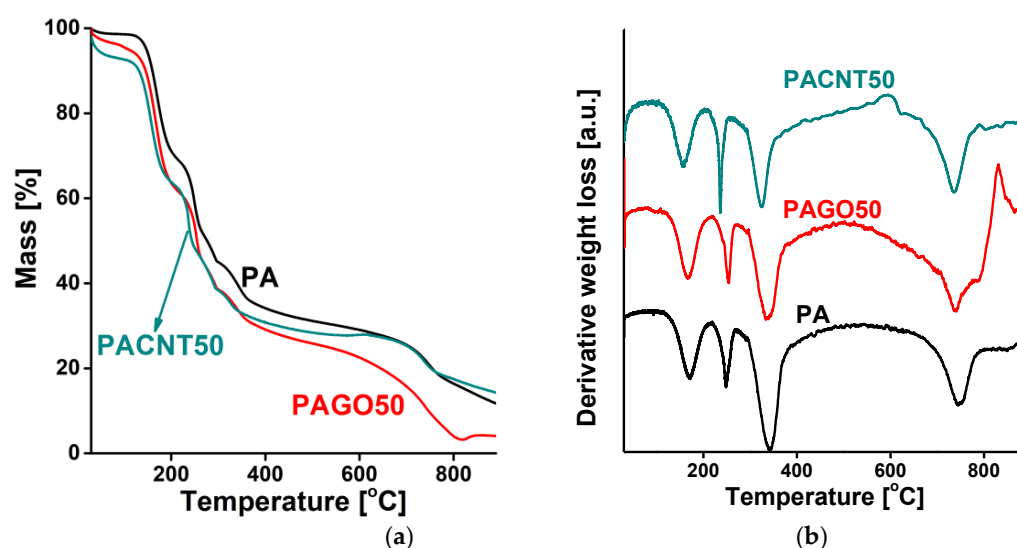


Figure 1. TG (a) and DTG (b) curves of the undoped polymer cryogel (PA), and the 50 mg CNP-doped polymer (PAGO50 and PACNT50) samples.

Figure 2 reveals the porous morphology of the carbon cryogels. Both CNPs seem well dispersed in the carbon matrix. The thermal treatment certainly reduces the GO that is incorporated into the carbon framework in the typical sheet-like form (Figure 2b). Similarly, CNTs added to the carbon cryogel kept their tubular shape (Figure 2c).

Low temperature N_2 adsorption isotherms and the respective pore size distribution curves for the GO- and CNT-doped carbons are shown in Figure 3. The numerical data deduced from these isotherms are presented in Table 1. According to the latest IUPAC classification, all the isotherms are a composite of Type II and IV, indicating the presence of micro-, meso- and macropores [40]. The H4 hysteresis loop having a sharp step-down around $p/p_0 = 0.45$ implies an interconnected pore network. Since the macropores are not totally filled with condensed nitrogen, the liquid equivalent volume $V_{0.98}$ was determined at $p/p_0 = 0.98$. According to Figure 3a, the surface-related properties of the carbon cryogel in the CAGO100 sample were most affected by addition of GO, both in the micro- and macropore regions, and 200 mg GO proved to be destructive due to the high amount of oxygen released by the GO during the heat treatment processes. The influence of CNT is more modest and slightly different. Adding only 50 mg CNT had an enhancing effect, but further addition of CNT gradually decreased both the apparent surface area and the pore volumes. The initial section of the CO_2 isotherms was utilized to reveal the

ultramicropore range, which is hardly accessible to the nitrogen molecules in cryogenic conditions. Figure 3b,d combines the pore size distributions in the ultramicropore and the micro-mesopore ranges. While in samples CAGO50 and CAGO100, GO increased the contribution of mesopores in the wider region (>10 nm), CNT had a widening effect in the narrow mesopore range. The distinctive impact of the GO and CNT may be related to their considerably different oxygen content as well as to their dissimilar geometry.

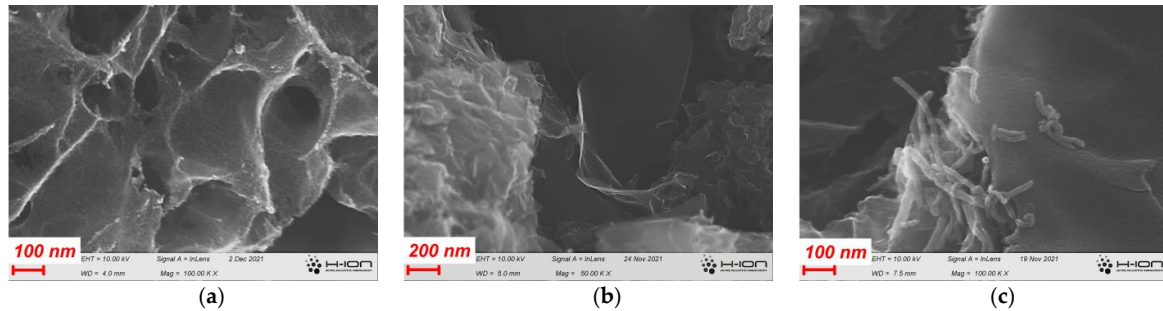


Figure 2. SEM image of the pristine carbon CA (a), GO-doped carbon CAGO50 (b) and CNT-doped carbon CACNT50 (c) samples.

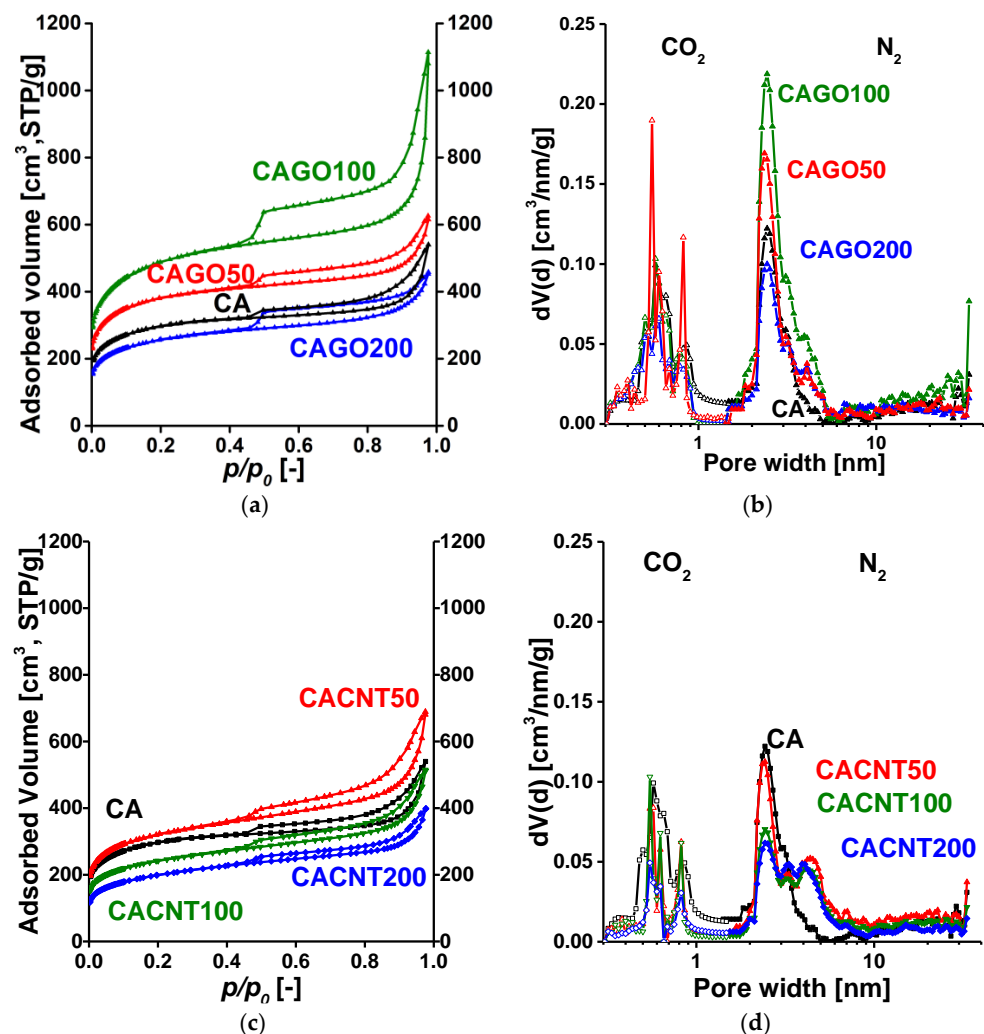


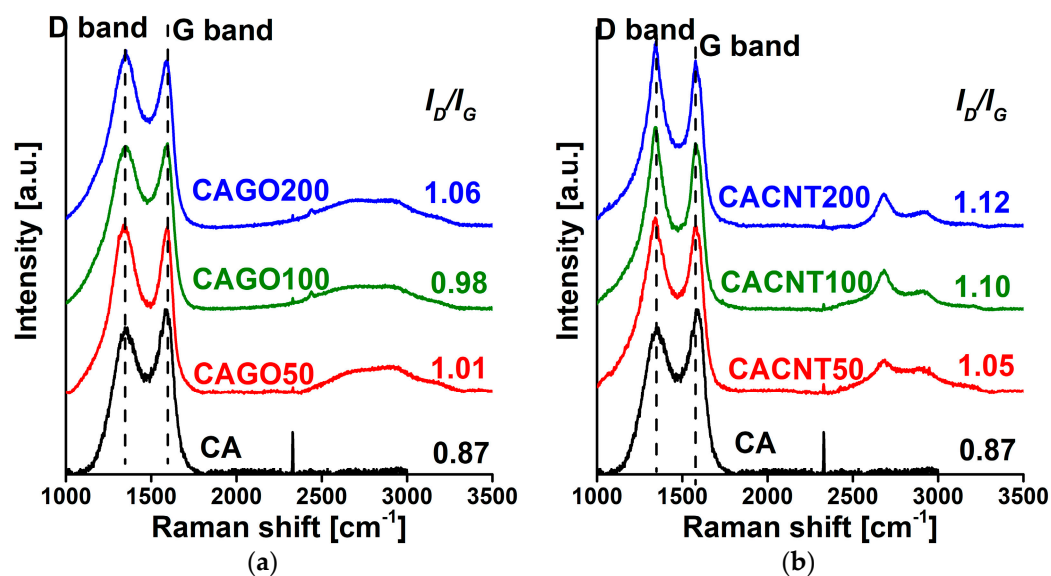
Figure 3. Low temperature N_2 adsorption/desorption isotherms of the GO- (a) and CNT- (b) doped carbon samples and their pore size distributions from $0^\circ C$ CO_2 adsorption (nonlinear density functional theory) and $-196.15^\circ C$ N_2 adsorption data (quenched solid density functional theory, slit/cylindrical pores) (c,d).

Table 1. Data deduced from the low temperature N₂ and 0 °C CO₂ isotherms *.

Sample	S_{BET} m ² /g	from N ₂			from CO ₂		
		$V_{0.98}$ cm ³ /g	W_0 cm ³ /g	%	V_{meso} cm ³ /g	$V_{ultra,DR}$ cm ³ /g	$V_{ultra,DFT}$ cm ³ /g
CA	1070	0.83	0.40	48	0.43	0.057	0.037
CAGO50	1408	0.95	0.56	59	0.39	0.049	0.027
CAGO100	1779	1.72	0.64	37	1.08	0.050	0.027
CAGO200	933	0.71	0.34	48	0.37	0.040	0.022
CACNT50	1169	1.07	0.43	40	0.64	0.032	0.018
CACNT100	880	0.79	0.32	41	0.47	0.028	0.016
CACNT200	727	0.62	0.26	42	0.36	0.020	0.013

* Apparent surface area from BET model; $V_{0.98}$ is the liquid volume of the gas adsorbed at $p/p_0 = 0.98$; W_0 micropore volume from DR model; $V_{meso} = V_{0.98} - W_0$ mesopore volume; $V_{ultra,DR}$: ultramicropore volume (<0.7 nm) from DR model; $V_{ultra,DFT}$: ultramicropore volume (<0.7 nm) from quenched solid density functional theory (QSDFT, CO₂ adsorbed on carbon at 0 °C).

The Raman spectra in Figure 4 show the iconic D (~1350 cm⁻¹; defects, edges and disordered carbon sites) and G (~1580 cm⁻¹, E_{2g} vibration of sp²-hybridized graphitic carbon) band regions typical of carbon materials [41]. Addition of either CNP enhanced the formation of defects, as demonstrated by the increasing I_D/I_G ratio with increasing amounts of additive. The effect is systematic and more pronounced in the CNT series.

**Figure 4.** Raman spectra of the GO- (a) and CNT- (b) doped carbons.

The effect of the incorporated CNPs on the surface composition was studied by XPS (Table 2). In the CAGO samples, the C content increases in CAGO50 and then decreases for the two other GO concentrations, while for the CACNT samples the C content increases slightly but systematically. Regarding the nitrogen content, its concentration decreases in both sets of samples but most notably for the CACNT samples. In contrast, the S content does not significantly change among the samples. While the incorporation of GO—except the CAGO50 sample—has no effect on the total heteroatom ratio, CNT addition gradually decreases the (O + N + S)/C ratio.

Table 2. Surface composition (atomic %) measured by XPS.

Sample	C	O	N	S	O/C	N/C	S/C	$\frac{O+N+S}{C}$	S/N
CA	90.6	3.3	5.1	1.0	0.036	0.056	0.011	0.104	0.196
CAGO50	92.0	3.1	3.7	1.3	0.034	0.039	0.014	0.087	0.361
CAGO100	90.7	4.1	4.1	1.2	0.045	0.045	0.013	0.104	0.293
CAGO200	90.4	3.7	4.4	1.4	0.041	0.049	0.015	0.105	0.318
GO	67.4	32.1	-	0.5	0.476	-	0.007	0.484	-
CACNT50	91.6	4.0	3.1	1.2	0.044	0.034	0.013	0.091	0.387
CACNT100	91.8	3.7	3.4	1.1	0.040	0.037	0.012	0.089	0.323
CACNT200	92.2	4.6	1.9	1.2	0.050	0.021	0.013	0.084	0.632
CNT	94.9	5.1	-	-	0.054	-	-	0.054	-

Figure 5 shows an example of the composite photoelectron lines (C1s, O1s, N1s and S2p) and their decomposition into the different chemical states. The binding energy ranges of the various states and their concentration are listed in Tables 3 and 4. Three different states of carbon, oxygen and nitrogen and two states of sulfur were distinguished in all the samples.

As XPS characterizes only the upper few nm of the samples, FTIR was also performed to reveal the composition in the deeper regions. The spectra for both sets of carbons are shown in Figure 6. The lines used for assignment are shown in Table 5 and the relative intensity ratios compared to the C=C signal are listed in Table 6. A systematic increase in the C=O/C=C and OH/C=C ratios was observed for both sets of samples, which may suggest that the thermal decomposition of both GO and the CNTs caused a relative increase in the oxygen functionalities C=O and OH with increasing CNP content. This agrees well with the chemical composition obtained from XPS.

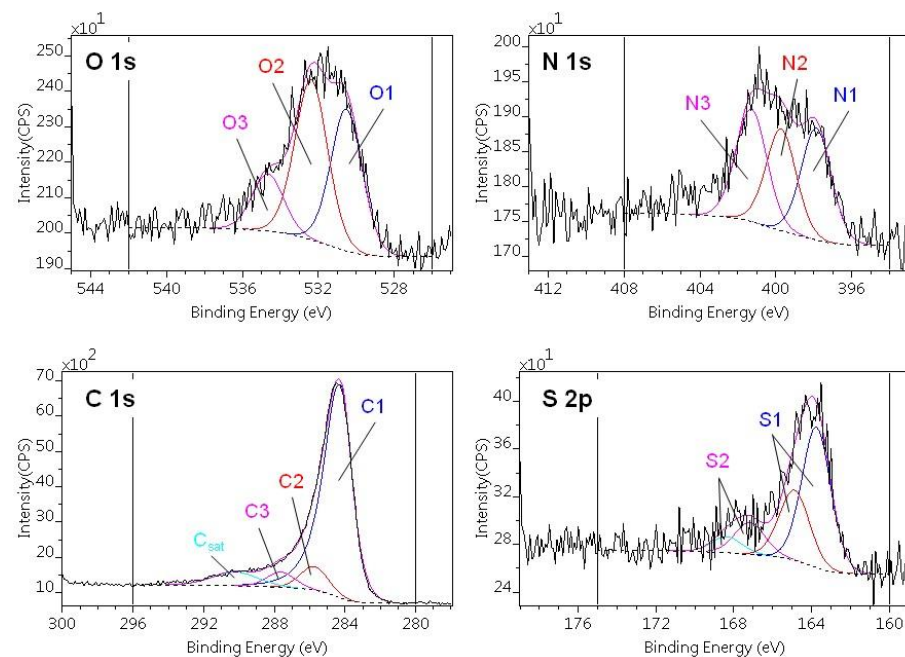


Figure 5. Decomposition of C1s, O1s, N1s and S2p regions of photoelectron spectra of the CACNT50 sample. Numerical data are given in Tables 3 and 4.

Table 3. Decomposition of C1s and O1s regions of photoelectron spectra: binding energy ranges, chemical state assignments and surface compositions (atomic %) [36].

	C1s			O1s		
	C1	C2	C3	O1	O2	O3
Chemical state	sp ² C=C	C–O C–N C–S	C=O O–C–O N–C–O	S–O	C–O–C C–OH C=O	OC–O–CO (H ₂ O)
Binding energy [eV]	284.3–284.4	285.7–285.8	287.5–287.9	530.2–530.6	532.1–532.5	533.9–534.3
CA	74.0	10.9	5.4	1.5	1.7	n.d.
CAGO50	78.8	7.4	5.5	1.9	1.3	n.d.
CAGO100	74.7	11.0	4.8	1.8	1.7	0.7
CAGO200	75.9	9.4	4.8	1.8	1.6	0.5
CACNT50	78.6	7.8	5.1	1.6	1.9	0.7
CACNT100	80.5	7.4	4.5	1.3	2.0	0.7
CACNT200	75.7	10.8	5.5	1.7	2.3	0.9

Table 4. Decomposition of N1s and S2p regions of photoelectron spectra: binding energy ranges, chemical state assignments and surface compositions (atomic %) [36].

	N1s			S2p	
	N1	N2	N3	S1	S2
Chemical state	C–N	OO–C–N	C–N ⁺	C–S	C–SO ₃
Binding energy [eV]	397.8–398.0	400.4–400.5	402.4–402.7	164.9–165.0	168.3–168.6
CA	2.3	2.3	0.8	0.9	0.2
CAGO50	1.6	1.7	0.6	1.2	n.d.
CAGO100	1.9	1.9	0.4	1.0	0.2
CAGO200	2.0	2.0	0.7	1.1	0.3
CACNT50	1.1	1.0	1.1	1.0	0.2
CACNT100	0.9	0.7	0.9	1.0	0.2
CACNT200	0.6	0.5	0.8	0.9	0.4

Table 5. Assignment of the FTIR peaks [42].

Wavenumber [cm ⁻¹]	Assignment
1750–1705	aromatic (1730–1705) and aliphatic (1750–1730) C=O stretching
1600–1400	C=C bond stretching in the aromatic ring
1350 ± 50	OH in-plane bending of phenol and alcohol groups
1260–1200	C–O stretching in phenols
1060–1035	C–O stretching in noncyclic acid anhydrides

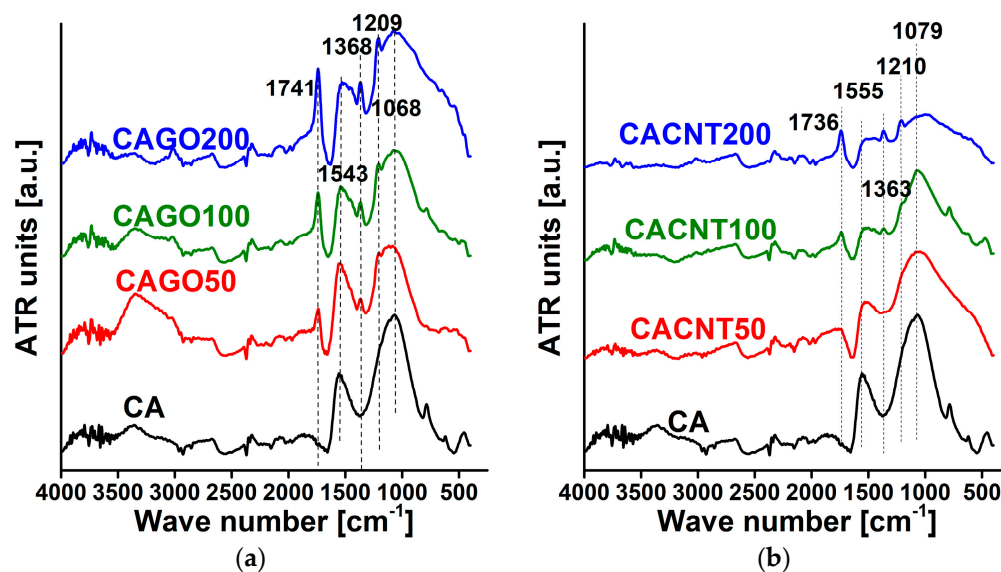


Figure 6. FTIR spectra of GO-doped carbons (a) and CNT-doped carbons (b).

Table 6. Intensity ratios of FTIR signal.

Sample	C=O/C=C	OH/C=C	C-O(H)/C=C	C-O-C/C=C
CA	0.19	0.50	1.33	1.69
CAGO50	0.53	0.62	1.10	1.17
CAGO100	0.93	0.78	1.31	1.51
CAGO200	1.17	1.02	1.55	1.60
CACNT50	0.53	0.81	1.50	1.86
CACNT100	0.91	1.00	1.73	2.68
CACNT200	1.33	1.33	1.72	1.89

3.2. Gas Storage and Separation Results

The potential of these carbons in gas separation was based on single gas adsorption measurements. The N₂, CO₂, H₂ and CH₄ adsorption isotherms of the various GO-doped carbon samples are presented in Figure 7. For easier comparison, only the adsorption branches are plotted and the gas uptakes are expressed in mmol/g. It should be noted that the effect of the incorporated GO varies from adsorbate to adsorbate. Incorporation of GO in the early stage of the synthesis affects not only the gel formation, but even more the porous texture and the surface chemistry in a sophisticated way. On comparing the N₂ and H₂ uptakes at −196.15 °C, it is clear that all the samples adsorb significantly more N₂ than H₂, as the boiling point of H₂, −252.9 °C, is much lower than the temperature of the uptake measurements. The almost tenfold difference indicates the potential of these carbon samples for N₂/H₂ separation at the temperature of these measurements. It is known that narrow micropores decorated with oxygen and nitrogen functional groups enhance CO₂ uptake [22]. The isotherms of CO₂ and CH₄ adsorption (0 °C) show that all samples adsorb more than twice as much CO₂ as CH₄ and CAGO50 attains the highest uptake for both gases at atmospheric pressure. This could indicate the potential of the GO-doped samples for CO₂/CH₄ separation.

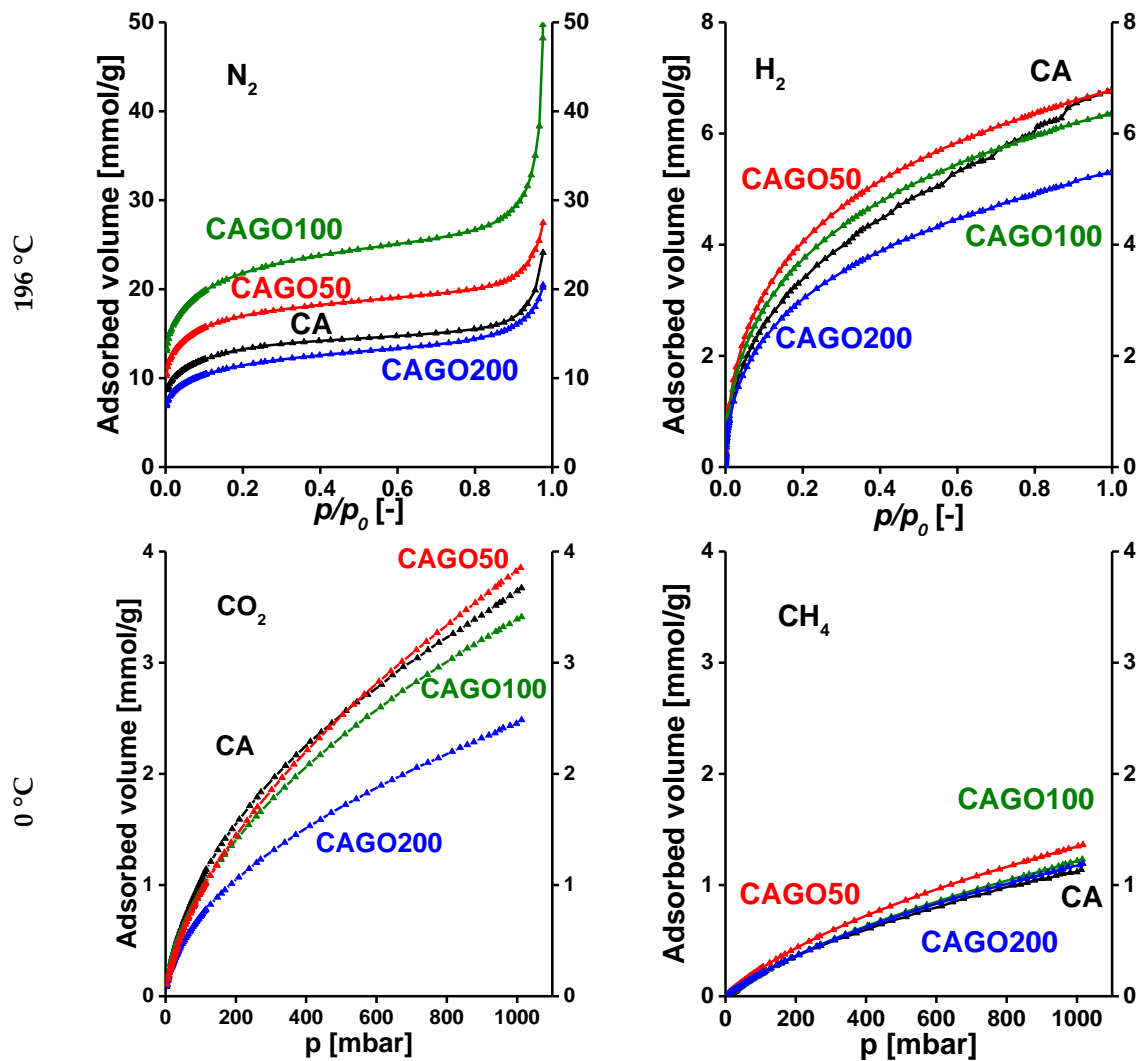


Figure 7. Adsorption isotherms of GO-doped carbon cryogels. N_2 and H_2 were measured at -196.15 °C, while CO_2 and CH_4 isotherms were measured at 0 °C.

Similarly, Figure 8 presents the N_2 , H_2 , CO_2 and CH_4 adsorption isotherms of the annealed CNT-doped carbons. Here, the sequence of the overall uptakes is similar at the two temperatures, respectively. Generally, the CNT-doped samples display a poorer adsorption performance (proportional to the incorporated CNT) than the undoped CA carbon. Only sample CACNT50 has somewhat higher uptakes for both gases measured at -196.15 °C.

In order to compare the interaction between the carbon surface and the probe gases, we used the corresponding fitting parameters of the DR and the Henry models. On the one hand, the slope of the linearized DR plot was used as follows,

$$\ln W = \ln W_0 - \left(\frac{RT}{E} \right)^2 \ln^2 \frac{p_0}{p} \quad (1)$$

where W is the actual filling of the micropore volume W_0 , E is the characteristic energy of the given system, p is the equilibrium pressure and p_0 is the saturation pressure of the probe gas at the temperature T of the measurement. On the other hand, the Henry constant K_H was determined, where the initial section of the isotherm was fitted to the Henry model as follows,

$$n = K_H \frac{p}{p_0} \quad (2)$$

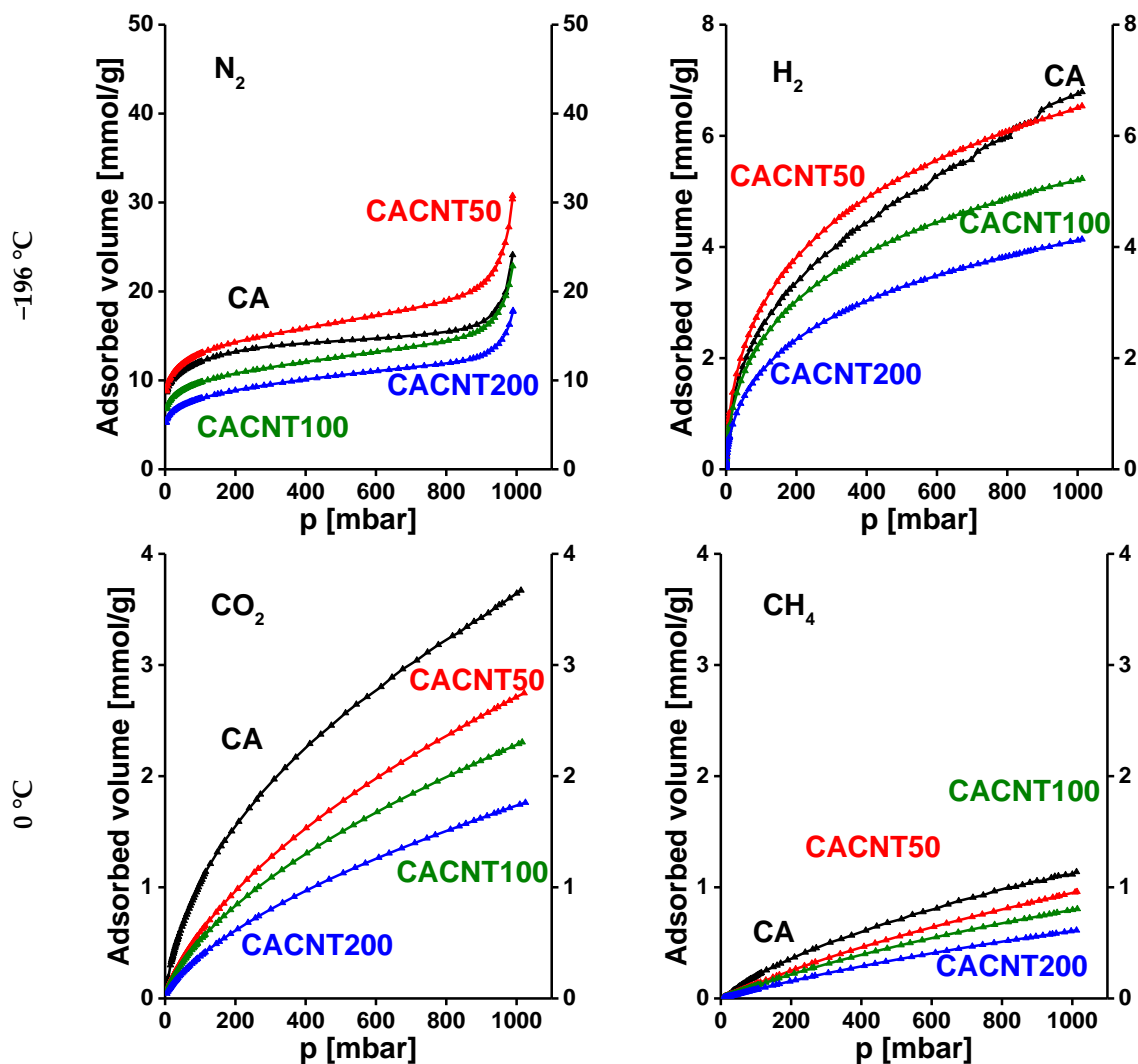


Figure 8. Adsorption isotherms of CNT-doped carbon cryogels. N₂ and H₂ were measured at −196.15 °C, while CO₂ and CH₄ isotherms were measured at 0 °C.

Here, *n* is the amount of gas adsorbed (mmol/g) at the corresponding relative pressure. The numerical data are given in Table 7.

Table 7. Interaction-related parameters and their ratios from the probe gas isotherms in Figures 7 and 8.

		CA	CAGO50	CAGO100	CAGO200	CACNT50	CACNT100	CACNT200	
−196 °C	N ₂	$\left(\frac{RT}{E}\right)^2$	0.0236	0.0254	0.0271	0.0278	0.0297	0.0292	0.0298
		K_H^*	0.151	0.284	0.338	0.156	0.213	0.152	0.140
	H ₂	$\left(\frac{RT}{E}\right)^2$	0.0978	0.106	0.108	0.0988	0.0842	0.116	0.0870
		K_H	0.543	0.661	0.541	0.437	0.430	0.329	0.241
0 °C	CO ₂	$\left(\frac{RT}{E}\right)^2$	0.212	0.196	0.182	0.163	0.197	0.198	0.201
		K_H	0.0186	0.0166	0.0190	0.0148	0.00950	0.00890	0.00620
	CH ₄	$\left(\frac{RT}{E}\right)^2$	0.551	0.239	0.195	0.251	0.236	0.239	0.220
		K_H	0.00210	0.00300	0.00210	0.00240	0.00140	0.00120	0.000900

* Expressed in mmol/(g·mbar).

The relative interactions were characterized by the ratio of the corresponding characteristic energies derived from the DR slopes and by the ratio of the K_H values (Figures 9 and 10). Comparison of the DR interactions reveals that the energy ratio governing the N_2/H_2 separation is higher than that of the CO_2/CH_4 separation. The addition of the nanoparticles does not enhance the energy ratios, but leads to a ca. 25% loss in the case of CO_2/CH_4 separation.

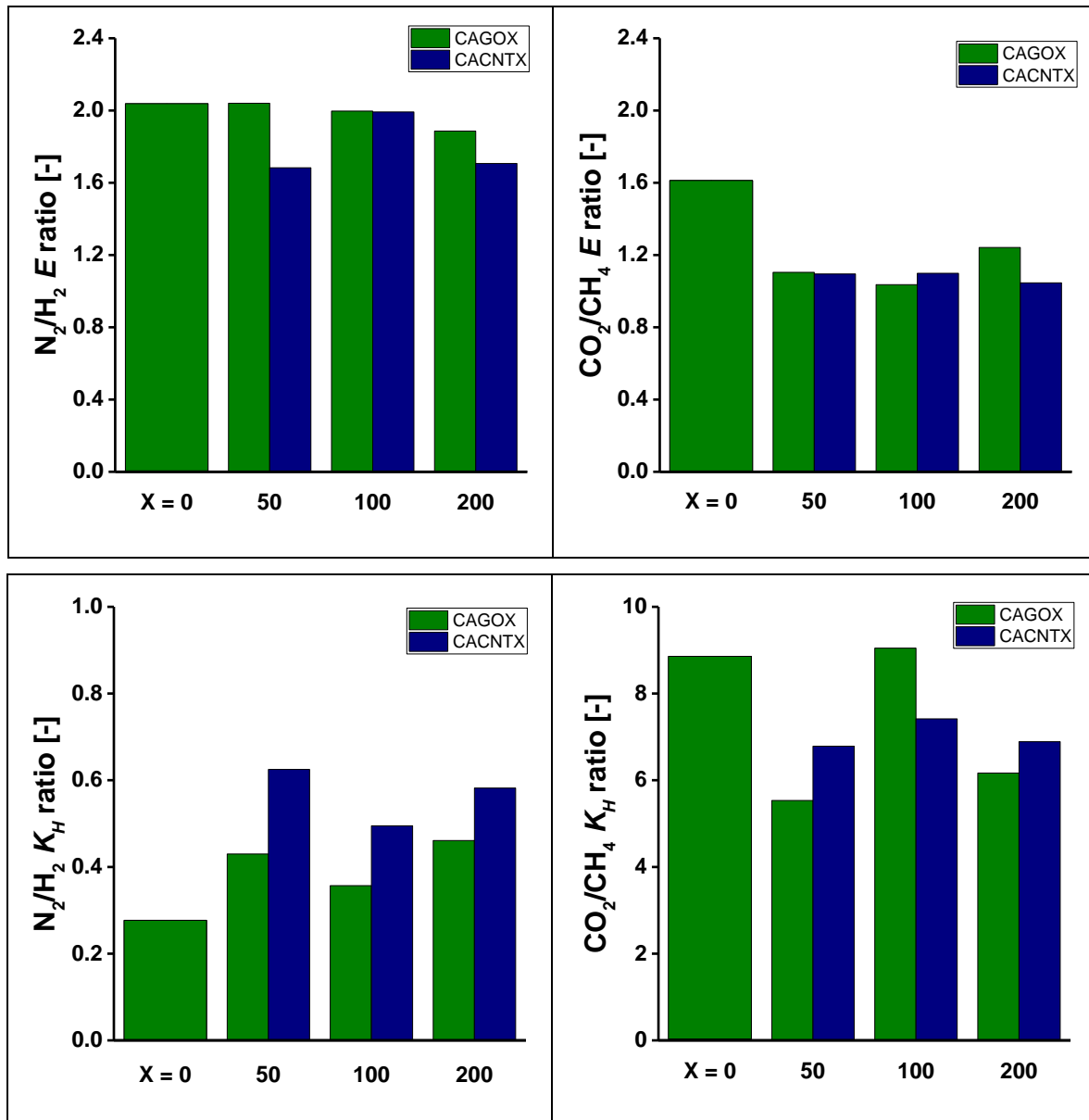


Figure 9. Comparison of characteristic parameters of gas/surface interactions.

The trend revealed of the Henry constant ratios are slightly different, as K_H is a more complex parameter, characterizing the distribution rather than the interaction itself. The Henry ratios are about ten times higher in the CO_2/CH_4 separation than in that of the N_2/H_2 . While the CNPs, particularly the nanotubes, have an enhancing effect for the latter, they do not improve this ratio for CO_2/CH_4 .

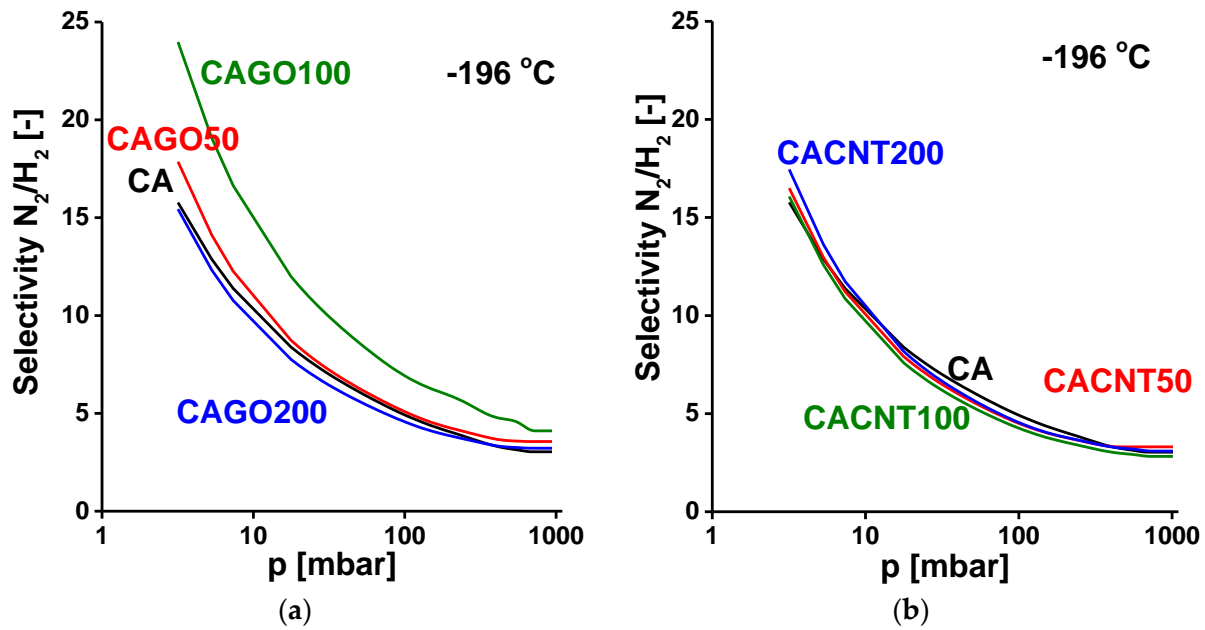


Figure 10. N_2/H_2 selectivity curves of GO-doped carbons (a) and CNT-doped carbons (b).

As in the work of Kamran et al. [43], IAST [29] was also used with the fitted adsorption data to determine and compare the N_2/H_2 and CO_2/CH_4 selectivity of the GO- and CNT-doped carbon samples. The N_2 adsorption isotherms were fitted to polynomial curves, while the CO_2 , CH_4 and H_2 adsorption isotherms were fitted to the single-site Langmuir–Freundlich model [44,45] as follows,

$$n = \frac{n_{sat} K p^m}{1 + K p^m} \quad (3)$$

where n is the adsorbed quantity at equilibrium pressure p , n_{sat} is the saturation capacity, K is the equilibrium constant of the Langmuir model and m (>1) is the Freundlich exponent. The selectivity curves for the N_2/H_2 system are shown in Figure 10, and those corresponding to the CO_2/CH_4 system are shown in Figure 11. In all the cases studied, the selectivity gradually reduces with increasing pressure. As expected, all the carbons adsorb nitrogen preferentially to hydrogen at -196 °C. The GO-doped carbons display a selectivity that is also influenced by the added GO. The CAGO100 sample is significantly better than the pristine CA carbon over the whole pressure range. For the CNT-doped carbons, all the selectivity curves lie close to that of the CA carbon, which indicates that the inclusion of CNTs did not affect the N_2/H_2 selectivity.

In CO_2/CH_4 separation at 0 °C (Figure 10), all the CNP-incorporated samples performed less well than the undoped CA carbon. Only sample CAGO100 reached a selectivity similar to CA in the lower pressure range. Apart from this case, the CNT-doped samples exhibited better selectivity than the GO family.

The trends observed from the three sets of comparisons confirm that relative adsorption and thus selectivity are a trade-off between multiple kinetics and diffusion-controlled processes (neither being independent of pore morphology and surface interactions). The most complex information is delivered by selectivity curves, but even they are only estimates that ignore any time-dependent and technical aspect of the separation.

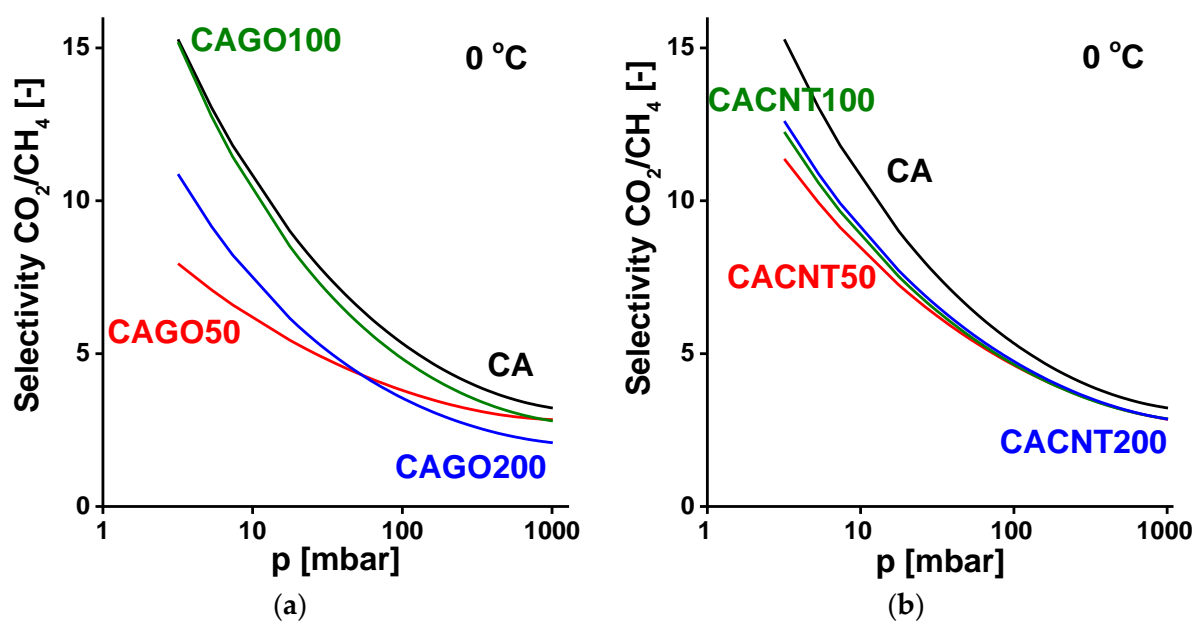


Figure 11. CO₂/CH₄ selectivity curves of GO-doped carbons (a) and CNT-doped carbons (b).

4. Conclusions

N, S double-doped porous carbon samples incorporating GO and CNT were successfully obtained from ι -carrageenan by applying urea as a nitrogen source during the synthesis. The carbon nanoparticles conserved their characteristic shape and were distributed homogeneously in the precursor gel. Their addition yielded a modified porous texture, particularly with GO with its significantly higher oxygen content. The highest apparent surface area and pore volume was found in the case of GO (sample CAGO100 possesses 1780 m²/g and 1.72 cm³/g, respectively), while with CNT a more modest improvement was achieved (CACNT50: 1169 m²/g and 1.07 cm³/g, respectively). The overall heteroatom concentration decorating the surface was slightly higher after the GO incorporation, as the nitrogen content was conserved more efficiently. The CNPs introduced further disorder into the matrix, as revealed by Raman spectroscopy. We can conclude that CNP, particularly GO incorporation, is more efficient in tuning the porous texture than the surface chemistry. Nitrogen and hydrogen isotherms measured at -196.15 °C and CO₂ and CH₄ isotherms at 0 °C were used to assess the effect of the CNPs on the selectivity of these carbons. The three different approaches applied to assess selectivity show different trends. The most complex method, IAST, revealed that incorporation of CNPs reduced rather than improved selectivity compared to neat CA itself in all the cases. The only exception was CAGO100, the best of the GO samples, which displayed enhanced selectivity in N₂/H₂ separation and a performance similar to CA for CO₂/CH₄. The estimates given here are based on the individual equilibrium isotherms and thus exclude any kinetic or diffusion-related mechanisms.

Author Contributions: Conceptualization: K.L.; methodology: M.M. and A.M.; investigation: S.K.S.A., M.M., S.K. and B.N.; resources: K.L.; writing—original draft preparation: K.L. and S.K.S.A.; writing—review and editing: K.L. All authors have read and agreed to the published version of the manuscript.

Funding: Financial support from the Hungarian Scientific Research Funds OTKA K128410 is acknowledged. The research is part of project no. BME-NVA-02, implemented with the support of the Ministry of Innovation and Technology of Hungary from the National Research, Development and Innovation Fund, and financed under the TKP2021 funding scheme. SKSA is grateful to the Stipendium Hungaricum scholarship program of the Hungarian Government.

Data Availability Statement: Data will be made available on request.

Acknowledgments: We extend our warm thanks to A. Farkas for his invaluable assistance in Raman spectroscopy and to G. Bosznai for his technical assistance.

Conflicts of Interest: The authors declare no conflict of interest.

References

1. Titirici, M.M.; White, R.J.; Falco, C.; Sevilla, M. Black perspectives for a green future: Hydrothermal carbons for environment protection and energy storage. *Energy Environ. Sci.* **2012**, *5*, 6796–6822. [[CrossRef](#)]
2. Karimi, M.; Shirzad, M.; Silva, J.A.C.; Rodrigues, A.E. Biomass/Biochar carbon materials for CO₂ capture and sequestration by cyclic adsorption processes: A review and prospects for future directions. *J. CO₂ Util.* **2022**, *57*, 101890. [[CrossRef](#)]
3. Praveen Kumar, D.; Ramesh, D.; Karuppasamy Vikraman, V.; Subramanian, P. Synthesis of carbon molecular sieves from agricultural residues: Status, challenges and prospects. *Environ. Res.* **2022**, *214*, 114022. [[CrossRef](#)] [[PubMed](#)]
4. Rehman, A.; Nazir, G.; Rhee, K.Y.; Park, S.J. A rational design of cellulose-based heteroatom-doped porous carbons: Promising contenders for CO₂ adsorption and separation. *J. Chem. Eng.* **2021**, *420*, 130421. [[CrossRef](#)]
5. Tan, Y.; Wang, X.; Song, S.; Sun, M.; Xue, Y.; Yang, G. Preparation of nitrogen-doped cellulose-based porous carbon and its carbon dioxide adsorption properties. *ACS Omega* **2021**, *6*, 24814–24825. [[CrossRef](#)] [[PubMed](#)]
6. Onyestyák, G.; László, K.; Rees, L.V.C. Molecular sieve honeycomb for air separation from *Picea abies*. *Helv. Chim. Acta* **2004**, *87*, 1888–1893. [[CrossRef](#)]
7. Alhwaige, A.A.; Agag, T.; Ishida, H.; Qutubuddin, S. Biobased chitosan hybrid aerogels with superior adsorption: Role of graphene oxide in CO₂ capture. *RSC Adv.* **2013**, *3*, 16011–16044. [[CrossRef](#)]
8. Shi, S.; Ochedi, F.O.; Cui, S.; Liu, Y. Removal of CO₂ from flue gas using seaweed porous carbons prepared by urea doping and KOH activation. *Energy Fuels* **2020**, *34*, 16411–16422. [[CrossRef](#)]
9. Yang, M.; Ma, C.; Xu, M.; Wang, S.; Xu, L. Recent advances in CO₂ adsorption from air: A review. *Curr. Pollut. Rep.* **2019**, *5*, 272–293. [[CrossRef](#)]
10. Lee, T.S.; Cho, J.H.; Chi, S.H. Carbon dioxide removal using carbon monolith as electric swing adsorption to improve indoor air quality. *Build. Environ.* **2015**, *92*, 209–221. [[CrossRef](#)]
11. Zhang, Z.; Zhou, J.; Xing, W.; Xue, Q.; Tan, Z.; Zhuo, S.; Qiao, S.Z. Critical role of small micropores in high CO₂ uptake. *Phys. Chem. Chem. Phys.* **2013**, *15*, 2523–2529. [[CrossRef](#)] [[PubMed](#)]
12. Villalobos, L.F.; Babu, D.J.; Hsu, K.-J.; Van Goethem, C.; Agrawal, K.V. Gas separation membranes with atom-thick nanopores: The potential of nanoporous single-layer graphene. *Acc. Mater. Res.* **2022**, *3*, 1073–1087. [[CrossRef](#)] [[PubMed](#)]
13. Zhu, L.; Shen, D.; Luo, K.H. A critical review on VOCs adsorption by different porous materials: Species, mechanisms and modification methods. *J. Hazard Mater.* **2020**, *389*, 122102. [[CrossRef](#)] [[PubMed](#)]
14. Jia, X.; Xu, S.; Cong, Y. Kinetics of spontaneous liquid-gas imbibition in carbon molecular sieves used for O₂/N₂ separation. *Microporous Mesoporous Mater.* **2017**, *241*, 185–191. [[CrossRef](#)]
15. Mohamed, A.R.; Mohammadi, M.; Darzi, G.N. Preparation of carbon molecular sieve from lignocellulosic biomass: A review. *Renew. Sustain. Energy Rev.* **2010**, *14*, 1591–1599. [[CrossRef](#)]
16. Villar-Rodil, S.; Navarrete, R.; Denoyel, R.; Albinia, A.; Paredes, J.I.; Martínez-Alonso, A.; Tascón, J.M.D. Carbon molecular sieve cloths prepared by chemical vapour deposition of methane for separation of gas mixtures. *Microporous Mesoporous Mater.* **2005**, *77*, 109–118. [[CrossRef](#)]
17. Marsh, H. *Rodríguez Reinoso: Activated Carbon*; Elsevier: Amsterdam, The Netherlands, 2006. [[CrossRef](#)]
18. Muhammad, R.; Nah, Y.-C.; Oh, H. Spider silk-derived nanoporous activated carbon fiber for CO₂ capture and CH₄ and H₂ storage. *J. CO₂ Util.* **2023**, *69*, 102401. [[CrossRef](#)]
19. Sevilla, M.; Al-Jumaily, A.S.M.; Fuertes, A.B.; Mokaya, R. Optimization of the pore structure of biomass-based carbons in relation to their use for CO₂ capture under low- and high-pressure regimes. *ACS Appl. Mater. Interfaces* **2018**, *10*, 1623–1633. [[CrossRef](#)]
20. Blankenship, T.S.; Balahmar, N.; Mokaya, R. Oxygen-rich microporous carbons with exceptional hydrogen storage capacity. *Nat. Commun.* **2017**, *8*, 1545. [[CrossRef](#)]
21. Park, J.; Attia, N.F.; Jung, M.; Lee, M.; Lee, K.; Chung, J.; Oh, H. Sustainable nanoporous carbon for CO₂, CH₄, N₂, H₂ adsorption and CO₂/CH₄ and CO₂/N₂ separation. *Energy* **2018**, *158*, 9–16. [[CrossRef](#)]
22. Ashourirad, B.; Arab, P.; Verlander, A.; El-Kaderi, H.M. From Azo-linked polymers to microporous heteroatom-doped carbons: Tailored chemical and textural properties for gas separation. *ACS Appl. Mater. Interfaces* **2016**, *8*, 8491–8501. [[CrossRef](#)]
23. Wang, X.; Sun, G.; Routh, P.; Kim, D.-H.; Huang, W.; Chen, P. Heteroatom-doped graphene materials: Synthesis, properties and applications. *Chem. Soc. Rev.* **2014**, *43*, 7067–7098. [[CrossRef](#)] [[PubMed](#)]
24. Sevilla, M.; Falco, C.; Titirici, M.M.; Fuertes, A.B. High-performance CO₂ sorbents from algae. *RSC Adv.* **2012**, *2*, 12792–12797. [[CrossRef](#)]
25. Liang, J.; Jiao, Y.; Jaroniec, M.; Qiao, S.Z. Sulfur and nitrogen dual-doped mesoporous graphene electrocatalyst for oxygen reduction with synergistically enhanced performance. *Angew. Chem. Int. Ed.* **2012**, *51*, 11496–11500. [[CrossRef](#)]
26. Bucior, B.J.; Chen, D.-L.; Liu, J.; Johnson, J.K. Porous carbon nanotube membranes for separation of H₂/CH₄ and CO₂/CH₄ mixtures. *J. Phys. Chem. C* **2012**, *116*, 25904–25910. [[CrossRef](#)]

27. Li, D.; Jia, Y.; Chang, G.; Chen, J.; Liu, H.; Wang, J.; Hu, Y.; Xia, Y.; Yang, D.; Yao, X. A defect-driven metal-free electrocatalyst for oxygen reduction in acidic electrolyte. *Chem* **2018**, *4*, 2345–2356. [[CrossRef](#)]
28. Samaniego Andrade, S.K.; Bakos, I.; Dobos, G.; Farkas, A.; Kiss, G.; Klébert, S.; Madarász, J.; László, K. Biomass related highly porous metal free carbon for gas storage and electrocatalytic applications. *Materials* **2021**, *14*, 3488. [[CrossRef](#)]
29. Myers, A.L.; Prausnitz, J.M. Thermodynamics of mixed-gas adsorption. *AIChE J.* **1965**, *11*, 121–127. [[CrossRef](#)]
30. Hummers, W.S.; Offeman, R.E. Preparation of graphitic oxide. *J. Am. Chem. Soc.* **1958**, *80*, 1339. [[CrossRef](#)]
31. Marcano, D.C.; Kosynkin, D.V.; Berlin, J.M.; Sinitskii, A.; Sun, Z.; Slesarev, A.; Alemany, L.B.; Lu, W.; Tour, J.M. Improved synthesis of graphene oxide. *ACS Nano* **2010**, *4*, 4806–4814. [[CrossRef](#)]
32. Tóth, A.; Voitko, K.V.; Bakalinska, O.; Prykhod'ko, G.P.; Bertóti, I.; Gun'ko, V.M.; László, K. Morphology and adsorption properties of chemically modified MWCNT probed by nitrogen, n-propane and water vapor. *Carbon* **2012**, *50*, 577–585. [[CrossRef](#)]
33. Brunauer, S.; Emmett, P.H.; Teller, E. Adsorption of gases in multimolecular layers. *J. Am. Chem. Soc.* **1938**, *60*, 309–319. [[CrossRef](#)]
34. Dubinin, M.M.; Radushkevich, L.V. The Equation of the characteristic curve of activated charcoal. *Dokl. Akad. Nauk. SSSR* **1947**, *55*, 327–329.
35. Landers, J.; Gor, G.Y.; Neimark, A.V. Density functional theory methods for characterization of porous materials. *Colloids Surf. A Physicochem. Eng.* **2013**, *437*, 3–32. [[CrossRef](#)]
36. Bertóti, I.; Mohai, M.; László, K. Surface modification of graphene and graphite by nitrogen plasma: Determination of chemical state alterations and assignments by quantitative X-ray photoelectron spectroscopy. *Carbon* **2015**, *84*, 185–196. [[CrossRef](#)]
37. Mohai, M. XPS MultiQuant: Multimodel XPS quantification software. *Surf. Interface Anal.* **2004**, *36*, 828–832. [[CrossRef](#)]
38. Evans, S.; Pritchard, R.G.; Thomas, J.M. Relative differential subshell photoionization cross-sections (MgK α) from lithium to uranium. *J. Electron. Spectrosc. Relat. Phenom.* **1978**, *14*, 341–358. [[CrossRef](#)]
39. Reilman, R.F.; Msezane, A.; Manson, S.T. Relative intensities in photoelectron spectroscopy of atoms and molecules. *J. Electron. Spectrosc. Relat. Phenom.* **1976**, *8*, 389–394. [[CrossRef](#)]
40. Thommes, M.; Kaneko, K.; Neimark, A.V.; Oliver, J.P.; Rodriguez-Reinoso, F.; Rouquerol, J.; Sing, K.S.W. Physisorption of gases, with special reference to the evaluation of surface area and pore size distribution (IUPAC Technical Report). *Pure Appl. Chem.* **2015**, *87*, 1051–1069. [[CrossRef](#)]
41. Wang, Y.; Alsmeyer, D.C.; McCreery, R.L. Raman spectroscopy of carbon materials: Structural basis of observed spectra. *Chem. Mater.* **1990**, *2*, 557–563. [[CrossRef](#)]
42. Smith, B.C. *Infrared Spectral Interpretation*; CRC Press: Boca Raton, FL, USA, 2018. [[CrossRef](#)]
43. Kamran, U.; Park, S.J. Acetic acid-mediated cellulose-based carbons: Influence of activation conditions on textural features and carbon dioxide uptakes. *J. Colloid Interface Sci.* **2021**, *594*, 745–758. [[CrossRef](#)]
44. Sips, R. On the structure of a catalyst surface. *J. Chem. Phys.* **1948**, *16*, 490–495. [[CrossRef](#)]
45. Sips, R. On the structure of a catalyst surface. II. *J. Chem. Phys.* **1950**, *18*, 1024–1026. [[CrossRef](#)]

Disclaimer/Publisher's Note: The statements, opinions and data contained in all publications are solely those of the individual author(s) and contributor(s) and not of MDPI and/or the editor(s). MDPI and/or the editor(s) disclaim responsibility for any injury to people or property resulting from any ideas, methods, instructions or products referred to in the content.